

Substructure in lensing clusters and simulations

Priyamvada Natarajan^{1,2}, Gabriella De Lucia³ and Volker Springel³

¹ *Department of Astronomy, Yale University, P. O. Box 208101, New Haven, CT, 06511-208101, USA*

² *Department of Physics, Yale University, P. O. Box 208120, New Haven, CT 06511-208120, USA*

³ *Max-Planck-Institut für Astrophysik, Karl-Schwarzschild-Strasse 1, Postfach 1317, D-85748 Garching bei München, Germany*

29 January 2019

ABSTRACT

We present high-resolution mass reconstructions for five massive cluster-lenses spanning a redshift range from $z = 0.18$ – 0.57 utilising archival *Hubble Space Telescope* (*HST*) data and applying galaxy-galaxy lensing techniques. These detailed mass models were obtained from the observations by combining constraints from the strong and weak lensing regimes. We ascribe local weak distortions in the shear maps to perturbations induced by the presence of galaxy haloes around individual bright early-type cluster member galaxies. This technique constrains the mass enclosed within an aperture for these subhaloes. We are sensitive to a specific mass range for these subhaloes, $10^{11} - 10^{12.5} M_{\odot}$, which we associate with galaxy-scale subhaloes. Adopting a parametric model for the subhaloes, we also derive their velocity dispersion function and the aperture radius function. The mass spectrum of substructure in the inner regions of the observed clusters is directly compared with that in simulated clusters extracted from the *Millennium Simulation*. The mass function, aperture radii and velocity dispersion function are compared in detail. Overall, we find good agreement between the distribution of substructure properties retrieved using the lensing analysis and those obtained from the simulation. We find that the fraction of total cluster mass associated with individual subhaloes within the inner $0.5 - 0.8 h^{-1} \text{Mpc}$ of our clusters ranges from 10–20 per cent, in broad agreement with simulations. Our work provides a powerful test of the ΛCDM model, which appears consistent with the amount of observed substructure in massive, lensing clusters based on present data.

Key words: gravitational lensing, galaxies: fundamental parameters, haloes, methods: numerical

1 INTRODUCTION

Gravitational lensing has emerged as one of the most powerful techniques to map mass distributions on a range of scales: galaxies, clusters and beyond. The distortion in the shapes of background galaxies viewed through foreground mass distributions is independent of the dynamical state of the lens, therefore, compared with other methods for mass estimation there are fewer biases in lensing mass determinations. Here, we focus on mapping in detail the mass distribution inside the inner regions of massive clusters of galaxies using Hubble Space Telescope (HST) observations. We exploit the technique of galaxy-galaxy lensing, which was originally proposed as a method to constrain the masses and spatial extents of field galaxies (Brainerd, Blandford & Smail 1996), which we have since extended and developed over the years to apply inside clusters (Natarajan & Kneib 1997; Natarajan et al. 1998; 2002a).

The detailed mass distribution within clusters and

specifically the fraction of the total cluster mass associated with individual galaxies has important implications for the frequency and nature of galaxy interactions in clusters (Merritt 1983; Richstone 1976; Farouki & Shapiro 1981; Moore et al. 1996; Ghigna et al. 1998; Okamoto & Habe 1999). Knowledge of the dynamical history of clusters enables a deeper understanding of the physical processes that shape their assembly and evolution. The discovery of strong evolution between $z \sim 0.5$ and the present-day in the morphological (and star-formation) properties of the galaxy populations in clusters has focused interest on environmental processes which could effect the gaseous component and dark matter halo of a cluster galaxy (e.g. Couch et al. 1994, 1998).

The global tidal field of a massive, dense cluster potential well is expected to be strong enough to truncate the dark matter halo of a galaxy whose orbit penetrates the cluster core. Therefore, probing the extents of galaxy haloes in clusters can provide invaluable clues to dynamically dominant processes in clusters. For instance, the survival of individual,

compact dark haloes associated with cluster galaxies suggests a high probability for galaxy–galaxy collisions within rich clusters over a Hubble time. However, since the internal velocity dispersions of cluster galaxies ($\lesssim 200 \text{ km s}^{-1}$) are significantly lower than their orbital velocities, these interactions are, in general, unlikely to lead to mergers, but rather encounters of the kind simulated in the galaxy harassment picture by Moore et al. (1996, 1998).

Previous work on galaxy–galaxy lensing in the moderate redshift field has identified a signal associated with massive haloes around typical field galaxies, extending to beyond¹ 100 kpc (e.g. Brainerd, Blandford & Smail 1996; Ebbels et al. 2000; Hudson et al. 1998; Hoekstra et al. 2004). In particular, Hoekstra et al. (2004) report the detection of a finite truncation radius of 185 ± 30 kpc via weak lensing by galaxies based on imaging data from the Red-Sequence Cluster Survey. Galaxy–galaxy lensing results from the analysis of the Sloan Digital Sky Survey data (McKay et al. 2002; Sheldon et al. 2004; Guzik & Seljak 2002) have contributed to a deeper understanding of the relation between mass and light. Similar analysis of galaxies in the cores of rich clusters suggests that the average mass-to-light ratio and spatial extent of the dark matter haloes associated with morphologically classified early-type galaxies in these regions may differ from those of field galaxies with comparable luminosity (Natarajan et al. 1998, 2002a). We find that at a given luminosity, galaxies in clusters have more compact halo sizes and lower masses (by a factor of 2–5) compared to their field counterparts. The mass-to-light ratios inferred for cluster galaxies in the V-band are also lower than those of field galaxies with comparable luminosity. This is a strong indication of the effect of the dense environment on the properties of dark matter haloes.

In this paper, we present a determination of the mass function and other detailed properties of substructure in clusters using galaxy–galaxy lensing techniques. A high resolution mass model tightly constrained by strong and weak lensing observations is constructed including individual cluster galaxies and their associated dark matter haloes. We show that over a limited mass range we can successfully construct the mass function of subhaloes inside clusters. In earlier work, we compared the mass function obtained from lensing with that extracted from a massive cluster simulated at extremely high resolution (Natarajan & Springel 2004). In this work, we are able to compare with a large ensemble of simulated clusters, significantly strengthening the statistical significance of our results.

N-body simulations represent an indispensable tool for investigating the non-linear growth of structures in its full geometrical complexity. The high numerical resolution achieved in recent years has demonstrated that the cores of dark matter haloes that fall into a larger system can survive for a relatively long time as self-gravitating objects orbiting in the smooth dark matter background of the system. A wealth of dark matter substructures is now routinely detected and studied with the aid of N-body simulations confirming that the existence of substructures is a generic

prediction of hierarchical structure formation in Cold Dark Matter (CDM) models.

The subhalo mass function (i.e. the abundance of dark matter substructure as a function of mass) represents an important prediction of hierarchical CDM structure formation models and has been subject of intense studies since the ‘dwarf galaxy crisis’ was identified (Moore et al. 1999; Klypin et al. 1999; Stoehr et al. 2003). Within a radius of $400 h^{-1}$ kpc, from the Milky Way, cosmological models of structure formation predict ~ 30 dark matter satellites with circular velocities in excess of 20 km s^{-1} and mass greater than $3 \times 10^8 M_{\odot}$. This number is significantly higher than the dozen or so satellites actually observed around our Galaxy. Different explanations have been suggested for this discrepancy. The missing satellites could for example be identified with the detected High Velocity Clouds (Maller & Bullock 2004). *Warm* or *self-interacting* dark matter could also selectively suppress power on the small scales, therefore reducing the predicted number of satellites (Spergel & Steinhardt 2000). The leading hypothesis however remains that the solution to this problem lies in astrophysical processes such as heating by a photo-ionising background that suppresses star formation in small haloes at early times (Bullock et al. 2000; Benson et al. 2002; Kravtsov et al. 2004). On the scale of galaxy clusters, many more dark matter structures are expected to host visible galaxies, thus making the comparison with expectations from numerical simulations less affected by uncertainties in the physics of galaxy formation. Full consistency is to be expected here, therefore providing an important test of the CDM paradigm.

Our innovative application of gravitational lensing enables a mapping of the distribution in mass of dark matter substructure (subhalo mass function) therefore allowing a direct comparison with results from numerical simulations. The strength of the lensing analysis presented here derives from the combination of both strong and weak lensing features which are used together to construct a high resolution mass map of a galaxy cluster. Anisotropies in the shear field (i.e. departure from the coherent tangential signal) in the vicinity of bright, early-type cluster members are attributed to the presence of these local potential wells. Statistically stacking this signal provides a way to quantify the masses associated with individual galaxy haloes. This is accomplished using a maximum likelihood estimator to retrieve characteristic properties for a typical subhalo in the cluster.

The comparison with clusters from the *Millennium Simulation* we use here is particularly powerful due to the large volume and high resolution of this simulation. The simulation used more than 10 billion particles to trace the evolution of the dark matter distribution in a cubic region of the Universe over 2 billion light-years on a side. This makes it an ideal data set for comparison with lensing clusters, providing dozens of highly resolved, massive lensing clusters out to redshifts $z \simeq 0.6$ and beyond.

The outline of this paper is as follows: in Section 2, we describe briefly the formalism for analysing galaxy–galaxy lensing in observed clusters including a synopsis of the adopted models. Section 3 presents the best-fit lens models and discusses the uncertainties and sources of error. A detailed comparison with clusters from the *Millennium Simulation* is presented in Section 4. The results of comparing the mass function of substructure, the distributions of aper-

¹ We adopt $h = H_0/100 \text{ km s}^{-1} \text{ Mpc}^{-1} = 0.7$ and $\Omega_{\Lambda} = 0.7$, and scale other published results to this choice of parameters.

ture radii and the velocity dispersions are discussed. Finally, we conclude with a discussion of the implications of our results for the Λ CDM model and the future prospects of this work in Section 5.

2 GALAXY-GALAXY LENSING IN CLUSTERS

2.1 Framework for analysis

In this section, we briefly outline the analysis framework, noting that further details can be found in earlier papers (Natarajan & Kneib 1997; Natarajan et al. 1998). For the purpose of extracting the properties of the subhalo population in clusters, a range of mass scales is modelled parametrically. The X-ray surface brightness maps of clusters suggest the presence of a smooth, dominant, large scale mass component. Clusters are therefore modelled as a super-position of a smooth large-scale potential and smaller scale potentials that are associated with bright early-type cluster members:

$$\phi_{\text{tot}} = \phi_{\text{smooth}} + \sum_i \phi_{p_i}, \quad (1)$$

where ϕ_{smooth} is the potential of the smooth component and ϕ_{p_i} is the potential of the subhalo associated with the i th galaxy, and is treated as perturber. The amplification matrix A^{-1} can be decomposed into contributions from the main clump and the perturbers:

$$A^{-1} = (1 - \kappa_{\text{smooth}} - \sum_i \kappa_{p_i}) I - \gamma_{\text{smooth}} J_{2\theta_{\text{smooth}}} - \sum_i \gamma_{p_i} J_{2\theta_{p_i}},$$

where κ is the magnification and γ the shear. The shear γ is in fact a complex number and is used to define the reduced shear \bar{g} , which is the quantity that is measured directly from the observed shapes of background galaxies. Similarly, the reduced shear can also be decomposed as

$$\bar{g}_{\text{tot}} = \frac{\bar{\gamma}}{1 - \kappa} = \frac{\bar{\gamma}_{\text{smooth}} + \sum_i \bar{\gamma}_{p_i}}{1 - \kappa_{\text{smooth}} - \sum_i \kappa_{p_i}}. \quad (2)$$

In the frame of an individual perturber j (and neglecting the effect of perturber i if $i \neq j$), this simplifies to:

$$\bar{g}_{\text{tot}}|_j = \frac{\bar{\gamma}_{\text{smooth}} + \bar{\gamma}_{p_j}}{1 - \kappa_{\text{smooth}} - \kappa_{p_j}}. \quad (3)$$

Restricting our analysis to the weak regime, and thereby retaining only the first order terms from the lensing equation for the shape parameters (e.g. Kneib et al. 1996), we have:

$$\bar{g}_I = \bar{g}_S + \bar{g}_{\text{tot}}, \quad (4)$$

where \bar{g}_I^2 is the distortion of the image, \bar{g}_S the intrinsic shape of the source, and \bar{g}_{tot} is the distortion induced by the lensing potentials.

In the local frame of reference of the perturbers, the mean value of the quantity \bar{g}_I and its dispersion can be computed in circular annuli (at radius r from the perturber centre) strictly in the weak-regime, assuming a constant value

$\gamma_c e^{i\theta_c}$ for the smooth cluster component over the area of integration. In the frame of the perturber, the averaging procedure allows efficient subtraction of the large-scale component, enabling the extraction of the shear component induced in the background galaxies only by the local perturber. The background galaxies are assumed to have intrinsic ellipticities drawn from a known distribution (see the next section for further details). Schematically, the effect of the cluster on the intrinsic ellipticity distribution of background sources is to cause a coherent displacement τ and the presence of perturbers merely adds small-scale noise to the observed ellipticity distribution.

The feasibility and robustness of signal detection has been amply demonstrated in earlier papers by Natarajan et al. The primary limitations in this analysis arise from the total number of distorted background galaxies, and the accuracy with which the smooth cluster component can be constrained using multiple images in the inner region. The partition into this smooth component and its effective subtraction in fact boosts the shear induced by the perturber. In particular, the shear induced by the subhalo has a $(\kappa_{\text{smooth}} + \kappa_{p_j})$ term in the denominator, which becomes non-negligible in the cluster centre. The subtraction of the larger-scale component reduces the noise in the polarisation measure by about a factor of two in cluster cores. This differenced averaging prescription for extracting the distortions induced by the possible presence of dark haloes around cluster galaxies is feasible with HST quality data as we have shown in earlier work (Natarajan et al. 1998, 2002a). The robustness of this technique also has been demonstrated in our earlier published work. Note here that it is the presence of the underlying large-scale smooth mass distribution (with a high value of κ_c) that enables the extraction of the weak signal riding on it. It is instructive to keep in mind that, in the regimes of interest discussed here, the distortion induced by the cluster-scale smooth component for a pseudo-isothermal elliptical component model (PIEMD) in the inner-most (with a velocity dispersion of 1000 km s⁻¹ and at $R/r_t \leq 0.1$) regions is typically of the order of 20 - 40 per cent or so in background galaxy shapes, and the perturbers produce distortions (smaller scale PIEMDs with a velocity dispersion of 220 km s⁻¹) of the order of 5 - 10 per cent, significantly more than in the case of weak-lensing by large scale structure or cosmic shear, wherein the distortions are of the order of 1 per cent.

2.2 Modelling the cluster

Each of the clusters studied in this paper preferentially probes the high mass end of the cluster mass function and has a surface mass density in the inner regions which is higher than the critical value, therefore producing a number of multiple images of background sources. By definition, the critical surface mass density for strong lensing is given by:

$$\Sigma_{\text{crit}} = \frac{c^2}{4\pi G} \frac{D_s}{D_d D_{ds}}, \quad (5)$$

where D_s is the angular diameter distance between the observer and the source, D_d the angular diameter distance between the observer and the deflecting lens, and D_{ds} the angular diameter distance between the deflector and the source. When the surface mass density in the cluster is in

² The measured image shape and orientation are used to construct a complex number whose magnitude is given in terms of the semi-major axis (a) and semi-minor axis (b) of the image and the orientation is the phase of the complex number.

excess of this critical value, strong lensing phenomena with high magnification are observed.

In general two types of lensing effects are produced – strong: multiple images and highly distorted arcs; and weak: small distortions in background image shapes determined by the criticality of the region. Viewed through the central, dense core region of the mass distribution, where $\kappa > 1$ strongly lensed features are observed. Note that the integrated lensing signal detected is due to all the mass distributed along the line of sight in a cylinder projected onto the lens plane. In this and all other cluster lensing work, the assumption is made that individual clusters dominate the lensing signal as the probability of encountering two massive rich clusters along the same line-of-sight is extremely small due to the fact that these are very rare objects in hierarchical structure formation models.

With our current sensitivity limits, galaxy-galaxy lensing within the cluster is primarily a tool to determine the total enclosed mass within an aperture. We lack sufficient sensitivity to constrain the detailed mass profile for individual cluster galaxies. With higher resolution data in the near future we will be able to obtain constraints on the slopes of mass profiles in subhaloes. In this paper, we therefore concentrate on pseudo-isothermal elliptical components (PIEMD models, derived by Kassiola & Kovner 1993) appropriately scaled for both the main cluster and the substructures. We find that the results obtained for the characteristics of the subhaloes (or perturbers) is largely independent of the form of the mass distribution (the aperture mass is comparable for the NFW and PIEMD models) used to model the smooth, large-scale component.

To quantify the lensing distortion induced by the global potential, both the smooth and individual galaxy-scale haloes are modelled self-similarly using a surface density profile, $\Sigma(R)$, which is a linear superposition of two PIEMD distributions,

$$\Sigma(R) = \frac{\Sigma_0 r_0}{1 - r_0/r_t} \left(\frac{1}{\sqrt{r_0^2 + R^2}} - \frac{1}{\sqrt{r_t^2 + R^2}} \right), \quad (6)$$

with a model core-radius r_0 and a truncation radius $r_t \gg r_0$. These parameters (r_t, r_0) are tuned for both the smooth component and the perturbers to obtain mass distributions on the relevant scales. The coordinate R is a function of x, y and the ellipticity,

$$R^2 = \frac{x^2}{(1+\epsilon)^2} + \frac{y^2}{(1-\epsilon)^2}, \quad \text{where } \epsilon = \frac{a-b}{a+b}. \quad (7)$$

The mass enclosed within radius R for the $\epsilon = 0$ model is given by

$$M(R) = \frac{2\pi\Sigma_0 r_0}{1 - \frac{r_0}{r_t}} \left[\sqrt{r_0^2 + R^2} - \sqrt{r_t^2 + R^2} + (r_t - r_0) \right]. \quad (8)$$

One of the attractive features of this model is that the total mass M is finite, $M \propto \Sigma_0 r_0 r_t$. Besides, analytic expressions can be obtained for all the quantities of interest, κ, γ and g , e.g.

$$\kappa(R) = \kappa_0 \frac{r_0}{(1 - r_0/r_t)} \left(\frac{1}{\sqrt{r_0^2 + R^2}} - \frac{1}{\sqrt{r_t^2 + R^2}} \right), \quad (9)$$

$$2\kappa_0 = \Sigma_0 \frac{4\pi G}{c^2} \frac{D_{ls} D_{ol}}{D_{os}}, \quad (10)$$

where D_{ls}, D_{os} and D_{ol} are the lens-source, observer-source and observer-lens angular diameter distances, respectively, which do depend on the choice of cosmological parameters. To obtain $g(R)$ knowing the magnification $\kappa(R)$, we solve Laplace's equation for the projected potential ϕ_{2D} , evaluate the components of the amplification matrix and then proceed to solve directly for $\gamma(R)$, and then $g(R)$:

$$\begin{aligned} \gamma(R) = & \kappa_0 \left[-\frac{1}{\sqrt{R^2 + r_0^2}} + \frac{2}{R^2}(\sqrt{R^2 + r_0^2} - r_0) \right. \\ & \left. + \frac{1}{\sqrt{R^2 + r_t^2}} - \frac{2}{R^2}(\sqrt{R^2 + r_t^2} - r_t) \right]. \end{aligned} \quad (11)$$

Scaling this relation by r_t gives for $r_0 < R < r_t$:

$$\gamma(R/r_t) \propto \frac{\Sigma_0}{\eta - 1} \frac{r_t}{R} \sim \frac{\sigma^2}{R}, \quad (12)$$

where σ is the velocity dispersion and for $r_0 < r_t < R$:

$$\gamma(R/r_t) \propto \frac{\Sigma_0}{\eta} \frac{r_t^2}{R^2} \sim \frac{M_{\text{tot}}}{R^2}, \quad (13)$$

where M_{tot} is the total mass. In the limit that $R \gg r_t$, we have

$$\gamma(R) = \frac{3\kappa_0}{2R^3} [r_0^2 - r_t^2] + \frac{2\kappa_0}{R^2} [r_t - r_0], \quad (14)$$

and as $R \rightarrow \infty$, $\gamma(R) \rightarrow 0$, $g(R) \rightarrow 0$ and $\tau(R) \rightarrow 0$, as expected.

It is further assumed that the ellipticity and the orientation of the dark matter subhaloes associated with the early-type cluster members is identical to that of the galaxies themselves. Additionally, in order to relate the light distribution to key parameters of the mass model above, we adopt a set of physically motivated scaling laws for the cluster galaxies (Brainerd et al. 1996):

$$\sigma_0 = \sigma_{0*} \left(\frac{L}{L_*} \right)^{\frac{1}{4}}; \quad r_0 = r_{0*} \left(\frac{L}{L_*} \right)^{\frac{1}{2}}; \quad r_t = r_{t*} \left(\frac{L}{L_*} \right)^{\alpha}. \quad (15)$$

These in turn imply the following scaling for the r_t/r_0 ratio η :

$$\eta = \frac{r_t}{r_0} = \frac{r_{t*}}{r_{0*}} \left(\frac{L}{L_*} \right)^{\alpha-1/2}. \quad (16)$$

The total mass M_{ap} enclosed within an aperture r_{t*} and the total mass-to-light ratio M/L then scale with the luminosity as follows:

$$M_{\text{ap}} \propto \sigma_{0*}^2 r_{t*} \left(\frac{L}{L_*} \right)^{\frac{1}{2}+\alpha}, \quad M/L \propto \sigma_{0*}^2 r_{t*} \left(\frac{L}{L_*} \right)^{\alpha-1/2}, \quad (17)$$

where α tunes the size of the galaxy halo. For $\alpha = 0.5$ the assumed galaxy model has constant M/L with luminosity (but not as a function of radius) for each galaxy; if $\alpha > 0.5$ ($\alpha < 0.5$) then brighter galaxies have a larger (smaller) haloes than the fainter ones. These scaling laws were empirically motivated by the Faber-Jackson relation for early-type galaxies (Brainerd, Blandford & Smail 1996). We assume these scaling relations and recognise that this could ultimately be a limitation of our model but the evidence at hand supports the fact that mass traces light efficiently both on cluster scales (Kneib et al. 2003) and on galaxy scales (McKay et al. 2002; Wilson et al. 2001).

2.2.1 The intrinsic shape distribution of background galaxies

As in all lensing work, it is assumed here as well that the intrinsic or undistorted distribution of shapes of background galaxies is known. This distribution is obtained from shape measurements taken from deep images of blank field surveys. Previous analysis of deep survey data such as the MDS fields (Griffiths et al. 1994) showed that the ellipticity distribution of sources is a strong function of the sizes of individual galaxies as well as of their magnitude (Kneib et al. 1996). For the purposes of our modelling, the intrinsic ellipticities for background galaxies are assigned in concordance with an ellipticity distribution $p(\tau_S)$ where the shape parameter τ is defined as $\tau = (a^2 - b^2)/(2ab)$ derived from the observed ellipticities of the CFHT12k data (see Limousin et al. 2005 for details):

$$p(\tau_S) = \tau_S \exp \left[- \left(\frac{\tau_S}{\delta} \right)^\nu \right]; \quad \nu = 1.15, \delta = 0.25. \quad (18)$$

Note that this distribution includes accurately measured shapes of galaxies of all morphological types. In the likelihood analysis this distribution $p(\tau_S)$ is the assumed prior, which is used to compare with the observed shapes once the effects of the assumed mass model are removed from the background images. We note here that the exact shape of the ellipticity distribution, i.e. the functional form and the value of δ and ν do not change the results, but alter the confidence levels we obtain. The width of the intrinsic ellipticity distribution on the other hand is the fundamental limiting factor in the accuracy of all lensing measurements.

2.2.2 The redshift distribution of background galaxies

While the shapes of lensed background galaxies can be measured directly and reliably by extracting the second moment of the light distribution, the precise redshift for each weakly object is in general unknown and therefore needs to be assumed. Using multi-waveband data from surveys such as COMBO-17 (Wolf et al. 2004), photometric redshift estimates can be obtained for every background object. Typically the redshift distribution of background galaxies is modelled as a function of observed magnitude $P(z, m)$. We have used data from the high-redshift survey VIMOS VLT Deep Survey (Le Fevre et al. 2004) as well as recent CFHT12k R-band data to define the number counts of galaxies, and the HDF prescription for the mean redshift per magnitude bin, and find that the simple parameterisation of the redshift distribution used by Brainerd, Blandford & Smail (1996) still provides a good description to the data.

For the normalised redshift distribution at a given magnitude m (in the given band) we therefore have

$$N(z)|_m = \frac{\beta \left(\frac{z^2}{z_0^2} \right) \exp \left[- \left(\frac{z}{z_0} \right)^\beta \right]}{\Gamma \left(\frac{3}{\beta} \right) z_0}, \quad (19)$$

where $\beta = 1.5$ and

$$z_0 = 0.7 \left[z_{\text{median}} + \frac{dz_{\text{median}}}{dm_R} (m_R - m_{R0}) \right], \quad (20)$$

with z_{median} being the median redshift, and dz_{median}/dm_R being the change in median redshift with say the R -band magnitude, m_R .

However, we note here in agreement with another recent study of galaxy-galaxy lensing in the field by Kleinheinrich et al. (2005), that the final results for the aperture mass presented here are primarily sensitive to the choice of the median redshift of the distribution rather than the individual assigned values.

2.3 The maximum-likelihood method

Parameters that characterise both the global component and the perturbers are optimised, using the observed strong lensing features - positions, magnitudes, geometry of multiple images and measured spectroscopic redshifts, when known, along with the smoothed shear field as constraints. Note that from the above parameterisation presented in the previous section, it is clear that we can optimise and extract values for the central velocity dispersion and the aperture scale (σ_{0*}, r_{t*}) for a typical L^* cluster galaxy.

A maximum-likelihood estimator is used to obtain significance bounds on fiducial parameters that characterise a typical L^* subhalo in the cluster. We have extended the prescription proposed by Schneider & Rix (1997) for galaxy-galaxy lensing in the field to the case of lensing by galaxy subhaloes in the cluster (Natarajan & Kneib 1997, Natarajan et al 1998). The likelihood function of the estimated probability distribution of the source ellipticities is maximised for a set of model parameters, given a functional form of the intrinsic ellipticity distribution measured for faint galaxies. For each ‘faint’ galaxy j , with measured shape τ_{obs} , the intrinsic shape τ_{S_j} is estimated in the weak regime by subtracting the lensing distortion induced by the smooth cluster model and the galaxy subhaloes,

$$\tau_{S_j} = \tau_{\text{obs}j} - \sum_i^{N_c} \gamma_{p_i} - \gamma_c, \quad (21)$$

where $\sum_i^{N_c} \gamma_{p_i}$ is the sum of the shear contribution at a given position j from N_c perturbers. This entire inversion procedure is performed numerically using code that builds on the ray-tracing routine LENSTOOL written by Kneib (1993). This machinery accurately takes into account the non-linearities arising in the strong lensing regime. Using a well-determined ‘strong lensing’ model for the inner regions of the clusters derived from the positions, shapes and magnitudes of the highly distorted multiple-imaged objects along with the shear field determined from the shapes of the weakly distorted background galaxies and assuming a known functional form for $p(\tau_S)$, the probability distribution for the intrinsic shape distribution of galaxies in the field, the likelihood for a guessed model is given by

$$\mathcal{L}(\sigma_{0*}, r_{t*}) = \Pi_j^{N_{\text{gal}}} p(\tau_{S_j}), \quad (22)$$

where the marginalisation is done over (σ_{0*}, r_{t*}) . We compute \mathcal{L} assigning the median redshift corresponding to the observed source magnitude for each arclet. The best fitting model parameters are then obtained by maximising the log-likelihood function with respect to the parameters σ_{0*} and r_{t*} . Note that the parameters that characterise the smooth component are also simultaneously optimised. The likelihood can also be marginalised over a complementary pair of parameters, e.g. using the luminosity scaling index α and the aperture mass M_{ap} directly. In this work, we explore both choices.

3 BEST-FIT LENSING MASS MODELS

A composite mass model is constructed for the clusters starting with the super-posed PIEMDs. The strong lensing data, i.e. the geometry, positions, relative brightness, redshifts and parities of the multiple images are used to obtain the mass enclosed within the Einstein radius which is used as an initial constraint for the integrated mass in the inner regions. The contribution to the shear and magnification from all potentials (large-scale and small-scale perturbers) is calculated at the location of every observed background source galaxy and the inversion of the lensing equation is performed. The observed shape and magnification of each and every distorted background galaxy is compared to that computed from the model and the subhalo mass distribution is modified iteratively until the best match between the observations and the model is found simultaneously for all background sources.

The basic steps of our analysis involve lens inversion, modeling and optimization, which are done using the LENSTOOL software utilities (Kneib 1993). These utilities are used to perform the ray tracing from the image plane to the source plane with a specified intervening lens. This is achieved by solving the lens equation iteratively, taking into account the observed strong lensing features, positions, geometries and magnitudes of the multiple images. In some cases, we also include a constraint on the location of the critical line (between 2 mirror multiple images) to tighten the optimization. In Figs. 1–5 of the Appendix, we show the iso-mass contours overlaid on their respective HST WFPC2 images. All the cluster galaxies included in the analysis have ellipses around them, and over-plotted are the critical curves (in yellow) for three different source redshifts ($z_s = 1, 2, 3$), the multiple images (in cyan) and the smoothed background shear field (in magenta) for the best-fit model. Additionally, we fix the core radius of an L^* subhalo to be 0.1 kpc, as by construction our analysis cannot constrain this quantity. In addition to the likelihood contours, the reduced χ^2 for the best-fit model is also robust. We describe some pertinent features of each cluster and their respective mass models below.

A 2218

Our best fit mass model for the cluster is bimodal, composed of two large scale clumps around the cD and the second brightest cluster galaxy (Fig. 1 of the Appendix). This model is an updated version of that constructed by Kneib et al. (1996). It includes 40 additional small-scale clumps that we associate with luminous early-type galaxies in the cluster core. Only about 10 per cent of the total cluster mass is in substructures, i.e. associated with galaxy scale haloes. The aperture mass, integrated over the truncation radius $r_{\text{ap}} = 40$ kpc, yields a characteristic mass of $1.4 \times 10^{12} M_\odot$, with a total mass-to-light ratio in the V-band of $\sim 5.8 \pm 1.5$ and a central velocity dispersion of about 180 km s^{-1} .

A 2390

The cluster has an unusual feature – a strongly lensed almost ‘straight arc’ (Pello et al. 1991) approximately 38 arcsec (~ 170 kpc) away from the central galaxy, in addition to many other arcs and arclets that have been utilised in our modeling. We find a best-fit mass model with two large-scale components, that yield a projected mass within the radius defined by the brightest arc of $\sim 1.8 \pm 0.2 \times 10^{14} M_\odot$. Our best-fit composite lensing model for A 2390 incorpo-

rates 40 perturbers associated with early-type cluster members whose characteristic parameters are optimized in the maximum-likelihood analysis. We show the equi-potentials of this mass model overlaid on the HST WFPC2 data in Fig. 2 of the Appendix, including those cluster galaxies selected as perturbers. We also show the critical curves for three different source redshifts ($z_s = 1, 2, 3$), the multiple images used to constrain the model, and the smoothed background shear field from the best-fit model. The integrated mass within the ~ 18 kpc tidal radius for a typical L^* cluster galaxy is about $6.4 \times 10^{11} M_\odot$ giving a total mass-to-light ratio in the V-band of about 4.2 ± 1.3 . Again, 90 per cent of the total mass of the cluster is consistent with being smoothly distributed.

Cl 2244–02

The best-fit lens model for this cluster has two components which both have fairly low velocity dispersions. This is the least massive lensing cluster in the sample studied here. The X-ray mass estimate from the *ASCA* data (Ota et al. 1998) is in good agreement with our best-fit lensing mass model. This is despite the fact that the X-ray temperature of Cl 2244–02 is at least a factor of two higher than that expected from the average luminosity-temperature relation.

The tidal truncation radius obtained for a typical L^* cluster galaxy in Cl 2244 is the largest in the sample studied here and is 55 ± 12 kpc. This is consistent with the fact that the central density in Cl 2244 is the lowest. The total mass-to-light ratio in the V-band for a fiducial L^* is 3.2 ± 1.2 . Approximately 20 per cent of the total mass is in substructure within the mass range $10^{11} - 10^{12.5} M_\odot$.

Cl 0024+16

Our best fit mass model for the inner regions takes into account the small scale dark haloes associated with the early-type members in the core, and requires a two component model for the sub-clusters (Fig. 4 in the Appendix). Integrating the best-fit mass model shown, we find that (i) about 10 per cent of the total cluster mass is in galaxy-scale haloes and (ii) the total mass estimate is in good agreement with that obtained by Kneib et al. (2003) where data from a much larger field of view were used.

Even on the large scales probed by Kneib et al. (2003) it was found that mass and light traced each other rather well at large radii. A typical L^* cluster galaxy was found to have a truncation radius of 45 ± 5 kpc, and a central velocity dispersion of $125 \pm 7 \text{ km s}^{-1}$.

Cl 0054–27

The lensing signal from Cl 0054–27 is best fit by a single smooth dark matter component and subhaloes associated with bright, early-type members making it the only unimodal cluster in the sample studied here. The mass enclosed within ~ 400 kpc is of the order of $1.8 \pm 0.4 \times 10^{14} M_\odot$. The best-fit mass model is plotted in Fig. 5 of the Appendix, with all the cluster galaxies included in the model shown explicitly.

The characteristic central velocity dispersion of a typical L^* galaxy in this cluster is higher than in A 2218, A 2390 or Cl 0024+16, all of which are by contrast bimodal in the mass distribution. In this cluster, about 20 per cent of the total mass is in substructure. However, Cl 0054–27 is the most distant cluster studied here and is likely to be still evolving and assembling, accounting for the high mass fraction in substructure.

Note here that the choice of α determines only the scaling of the outer radius of a fiducial subhalo with luminosity. With the data used in this paper it is not possible to distinguish between various values of α - some values are clearly more physical than others. Therefore, this implies that we are sensitive to the integrated mass within an aperture that is determined primarily by the anisotropy in the shear field and not by the details of how the subhalo masses are truncated. We also find that out to 500 kpc in all clusters only 10–20 per cent of the total mass is associated with galaxy haloes. At this radius (to which we are limited due to the size of the HST WFPC2 fields), most of the mass is in the large-scale component. This fraction is likely to be a strong function of cluster-centric radius. The dependence of these aperture radii with distance from the cluster can be explored with wide-field HST data and we are in the process of doing so for the cluster Cl0024+16 (Natarajan et al. 2006).

3.1 Results from the lens models

We successfully construct high resolution mass models for all five clusters from the unambiguous galaxy-galaxy lensing signal detected using the maximum-likelihood analysis. We constrain the mass enclosed within an aperture for a fiducial halo. All our lens models are plotted in Figs. 1–5 of the Appendix. The maximum-likelihood analysis yields the following: (i) the mass-to-light ratio in the V -band of a typical L^* galaxy does not evolve significantly as a function of redshift, (ii) the fiducial truncation radius of an L^* galaxy varies from about 20 kpc to 70 kpc depending on the cluster (iii) the typical central velocity dispersion is roughly 180 km s^{-1} . In Fig. 1, we show the recovered parameters (σ_0^* , r_{t*}) for an L^* galaxy from the maximum-likelihood analysis. For the galaxy mass model adopted in our analysis, the total mass of an L^* galaxy varies from $\sim 4.9 \times 10^{11} M_\odot$ to $\sim 1.4 \times 10^{12} M_\odot$. The mass-to-light ratios quoted here (see Table 1 in the Appendix) take passive evolution of elliptical galaxies into account as given by the stellar population synthesis models of Bruzual & Charlot (2003), therefore any detected trend reflects pure mass evolution. The mass obtained for a typical bright cluster galaxy by Tyson et al. (1998) using only strong lensing constraints inside the Einstein radius of the cluster Cl0024+1654, at $z = 0.41$, is consistent with our results. All error bars quoted here are $\sim 3\sigma$.

By construction, the maximum-likelihood technique presented here provides the mass spectrum of subhaloes in the cluster directly. Note that as stated before, in performing the likelihood analysis to obtain characteristic parameters for the subhaloes in the cluster, it is assumed that light traces mass. This is an assumption that is well supported by galaxy-galaxy lensing studies in the field (Wilson et al. 2001) as well as in clusters (Clowe & Schneider 2002). In fact, all lens modeling and rotation curve measurements suggest an excess of baryons in the inner regions. Note however that for our choice of mass model (the PIEMD) the mass to light ratio is not constant with radius within an individual galaxy halo. Since the procedure involves a scaled, self-similar mass model that is parametric, we obtain a mass estimate for the dark haloes (subhaloes) as a function of the luminosity of the early-type galaxy hosted by them. This provides us with a clump mass spectrum. We surmise that truncation by the

cluster causes these galaxy halo masses to be lower than that of equivalent luminosity field galaxies at comparable redshifts obtained from galaxy-galaxy lensing. The fraction of mass in these clumps is only 10–20 per cent of the total mass of the cluster within the inner $500 h^{-1} \text{ kpc}$ of these high central density clusters. The remaining 80–90 per cent of the cluster mass is consistent with being smoothly distributed (in clumps with mass $M < 10^{10} M_\odot$, the precise composition of this component depends on the hitherto unknown nature of dark matter. Note that the upper and lower limits on the mass spectrum vary from cluster to cluster due to the difference in the luminosity functions of cluster galaxies. These mass functions and other detailed properties of the substructure can now be directly compared to the subhalo mass functions of dark matter haloes taken from the Millennium simulation, the results of which are presented in Section 4.

3.1.1 Uncertainties, sources of error and robustness of the lens models

The following tests were performed for each cluster, (i) choosing random locations (instead of bright, early-type cluster member locations) for the perturbers; (ii) scrambling the shapes of background galaxies; (iii) choosing to associate the perturbers with the 40 faintest (as opposed to the 40 brightest) galaxies; (iv) randomly selecting known cluster galaxies as perturbers; (v) selecting late-type galaxies. None of the above cases (i)–(v) yields a convergent likelihood map, in fact all that is seen in the resultant 2-dimensional likelihood surfaces is noise.

The robustness of our results has been extensively tested, however there are a couple of caveats that we ought to mention. As outlined above, in this galaxy-galaxy lensing technique we are only sensitive to a restricted mass range in terms of secure detection of substructure. This is due to the fact that we are quantifying a differential signal above the average tangential shear induced by a cluster, and we are inherently limited on by the average number of distorted background galaxies that lie within the aperture scale radii of cluster galaxies. This trade-off between requiring a sufficient number of lensed background galaxies in the vicinity of the subhaloes and the optimum locations for the subhaloes leads us to choose the brightest 40 early-type cluster galaxies for each lens. With deeper, wider and more numerous images of clusters, expected in the future with a wide-field imager in space such as the SNAP mission (Aldering et al. 2003), this technique can be pushed much further to probe down to lower masses in the mass function. It is possible that the bulk of the mass in subhaloes is in lower mass clumps (which in this analysis is essentially accounted for as part of the smooth component) and are in fact anti-correlated with positions of early-type galaxies.

Our results still hold true since we are filtering out only the most massive clumps via this technique. Note that one of the null tests performed above, associating galaxy haloes with random positions in the cluster (and not with the locations of bright, early-type galaxies) resulted in pure noise. Even if we suppose that the bulk of the dark matter is associated with say, dwarf/very low surface brightness galaxies in clusters, then the spatial distribution of these galaxies is required to be fine-tuned such that these effects do not show

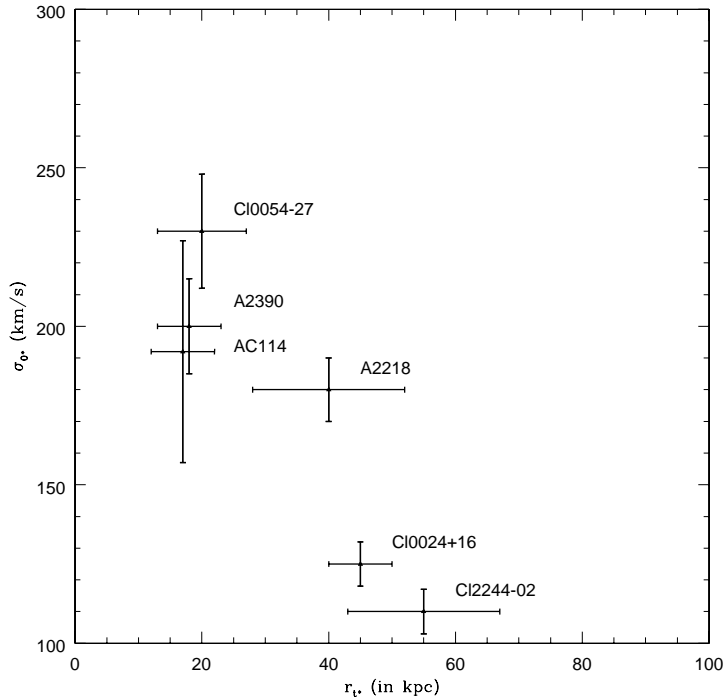


Figure 1. The retrieved best-fit values for the 2 parameters that were marginalised over in the likelihood analysis, the central velocity dispersion and aperture radius for an L^* galaxy in each of the clusters. Included is the previously published data point for AC114. The error bars are 3σ for both σ_{0*} and r_{t*} . It is these error bars that translate into a factor of 2 error in the total aperture mass.

up in the shear field in the inner regions, implying that if at all they are likely to be more significant repositories of mass perhaps in the outskirts of clusters.

Guided by the current theoretical understanding of the assembly of clusters, dwarf galaxies are unlikely to survive in the high density core regions of galaxy clusters studied here. Studies such as the one presented here when applied on larger scales to distances of a few Mpc from the cluster centre will enable an understanding of the role of environment in mass stripping of these haloes. In a recent study, Limousin et al. (2006) track the mass inferred for a fiducial cluster galaxy as a function of cluster-centric distance out to twice the virial radius. Using ground-based data they do not detect any significant variation in mass, however, using mosaiced HST images Natarajan et al. (2006), find that a typical L^* galaxy-halo has higher aperture mass in the outskirts of the cluster.

The principal sources of error in the above analysis are (i) shot noise – we are inherently limited by the finite number of sources sampled within a few tidal radii of each cluster galaxy; (ii) the spread in the intrinsic ellipticity distribution of the source population; (iii) observational errors arising from uncertainties in the measurement of ellipticities from the images for the faintest objects and (iv) contamination by foreground galaxies mistaken as background. As mentioned in Section 2.2.2, the partitioning of mass into subhaloes and the smooth component as done here is largely independent of the $N(z)$ of background galaxies.

In terms of the total contribution to the error budget, based on simulations we find that the shot noise is the most

significant source of error, amounting to ~ 50 per cent; followed by the width of the intrinsic ellipticity distribution which contributes ~ 20 per cent, and the other three sources together contribute ~ 30 per cent. This elucidates the future strategy for such analyses – going significantly deeper and wider in terms of the field of view is likely to provide considerable gains. Mosaic-ed ACS images are the ideal data sets for this galaxy-galaxy lensing analyses, and such work is currently in progress.

4 COMPARISON WITH N-BODY SIMULATIONS

In this section, we present a comparison between the properties of the subhaloes determined using the lensing analysis detailed above and results from N-body simulations. For this study, we make use of the *Millennium Simulation*, recently carried out by the Virgo Consortium and described in detail in Springel et al. (2005). The simulation follows $N = 2160^3$ particles within a comoving box of size $500 h^{-1} \text{Mpc}$ on a side. With a particle mass of $8.6 \times 10^8 h^{-1} M_\odot$ and a spatial resolution of $5 h^{-1} \text{kpc}$, the Millennium Simulation provides an unprecedented combination of high resolution and large volume that allows the formation of rare objects – like massive lensing clusters – to be followed in a representative fashion. It therefore represents an ideal simulation to compare with observations as a relatively large sample of massive, lensing clusters can be extracted over the redshift range probed by the observations. For the 64 time slices produced by the simulation, embedded substructures within

dark matter haloes were identified with the algorithm SUBFIND (Springel et al. 2001). In brief, the algorithm decomposes a given particle group (previously identified with a standard friends-of-friends algorithm) into a set of disjoint substructures, each of which is identified as a locally overdense region in the density field of the background halo. After the regions containing substructure candidates have been identified, an unbinding procedure is employed to iteratively reject all particles with positive total energy. All substructures that survive the unbinding procedure, and still have at least 20 self-bound particles, are considered to be genuine substructures. We refer to the original paper for more details on the algorithm. We note however that the identification of subhaloes within haloes represents a difficult technical problem. A variety of different algorithms have been developed in order to accomplish this task (e.g. Gottlöber et al. 1998; Klypin et al. 1999; Springel et al. 2001; Weller et al. 2005), but unfortunately little work has been done so far to compare the properties of subhaloes identified with different methods, so that the systematic effects and differences inherent in these methods are largely unknown.

In order to carry out our comparison with lensing results, we have selected all haloes with $M_{200} \geq 8 \times 10^{14} M_{\odot}$ from the simulation box at the snapshots corresponding to the redshifts of the lensing clusters (see Table 1). We find 17, 15, and 12 very massive haloes at the redshifts of the clusters A 2218, A 2390, and Cl 2244–02 respectively. Massive cluster haloes are on the tail of the mass function in a Λ CDM Universe and their number decreases rapidly with increasing redshift. For Cl 0024+16 and Cl 0054–27, we have therefore combined two adjacent snapshots (in both cases the redshift of the observed cluster lies in between those of the used snapshots), which led to 12 and 6 candidates, respectively.

For each cluster halo, we have analysed the distribution of the subhalo properties by projecting along the x , y , and z axes and keeping only subhaloes within 1 Mpc from the cluster centre, identified with the position of the most bound particle. The distributions we discuss in the following are then the average over the three projections of all the haloes identified for each redshift.

4.1 The mass function of substructures

As mentioned in Sec. 1, a direct mapping of the substructure mass function is ultimately of interest since it provides an important test of the Λ CDM paradigm. In addition, it is intimately connected to the galaxy formation process: comparison of the dark halo mass function with the observed luminosity function of galaxies can provide valuable insights into the physical processes driving galaxy formation and evolution. In this work, we restrict ourselves to a comparison of the properties of the dark matter component. A yet more detailed comparison for A 2218 in terms of observable galaxy properties by means of simulations and semi-analytic techniques is presented elsewhere (De Lucia & Natarajan 2006).

In Fig. 2 we compare the substructure mass function retrieved from the galaxy-galaxy lensing analysis (hashed histograms) with the results from the numerical simulation. The black solid line in each panel represents the average over the three orthogonal projections of all the massive haloes identified for each redshift. The grey filled histograms show

for each value of the subhalo mass, the minimum and maximum number of substructures found in the simulated clusters. We note that the mass of the subhaloes used to build the grey histogram in Fig. 2 is defined in terms of the total number of particles they contain, and has been multiplied by a correction factor of 2, as discussed below. As shown in Fig. 1, the error bars in σ_{0*} and r_{t*} retrieved from the lensing observations translate into a factor of 2 error in the aperture mass of substructures.

When taken at face value this correction factor of 2 would signal a discrepancy between the simulation and lensing results. However, we argue that it is much more likely that the difference is dominated by systematic effects in the measurement of substructure masses in the simulation, and possibly also in the lensing analysis. Note that the algorithm SUBFIND identifies substructures as overdense regions bounded by an isodensity surface where the density equals the local value of the background host halo. Because of this criterion for identifying substructure, it is likely that our subhalo masses are biased low, because only the ‘tip of the iceberg’ is seen. This effect should increase the closer a subhalo is located to the centre. Other algorithms for identifying substructures suffer from this problem in similar ways. However, the uniformity of the measured slopes for the subhalo mass function from different studies (De Lucia et al. 2004; Diemand et al. 2004) suggest that these differences can be accounted for through simple scale factors, at least at a statistical level.

In addition, it is likely that there are some systematic effects in the mass estimate based on the lensing analysis as well. Here a systematic overestimate appears more likely, arising for example if the most massive substructures correspond to haloes that have fallen in most recently, as indicated by recent numerical studies (De Lucia et al. 2004; Gao et al. 2004). As for the mass reconstruction technique employed here, biases can also be introduced due to the possible existence of substructure along the line of sight, not in the lens plane but behind it (Natarajan 2006). Fig. 2 also shows that there is a large scatter among simulated clusters and since the number of substructures in the observable mass range is quite small, we also expect large system-to-system variations between different observed systems. Besides, as shown in Table 1, the subhalo masses are uncertain to within a factor of 2 from the galaxy-galaxy lensing analysis, based on the observational limitations from current data.

We note here in our preliminary comparison of the lensing derived mass function with that extracted from the simulation of a single, massive cluster (Natarajan & Springel 2004), we had found excellent agreement without the need for a mass correction factor. However, it turns out that this result was influenced by not correctly taking into account the spatial geometry of the HST field. When this effect is appropriately included, our present results are consistent with this earlier work, and a mass correction factor of 2 is required to obtain quantitative consistency. Note that this is within the limits of the systematic uncertainties both of the substructure mass detection in the simulations as well as those from the lensing analysis.

Overall, it is therefore remarkable that we find very good qualitative agreement in the mass range sampled by the lensing analysis, and very good quantitative agreement as well when the systematic biases are approximately cor-

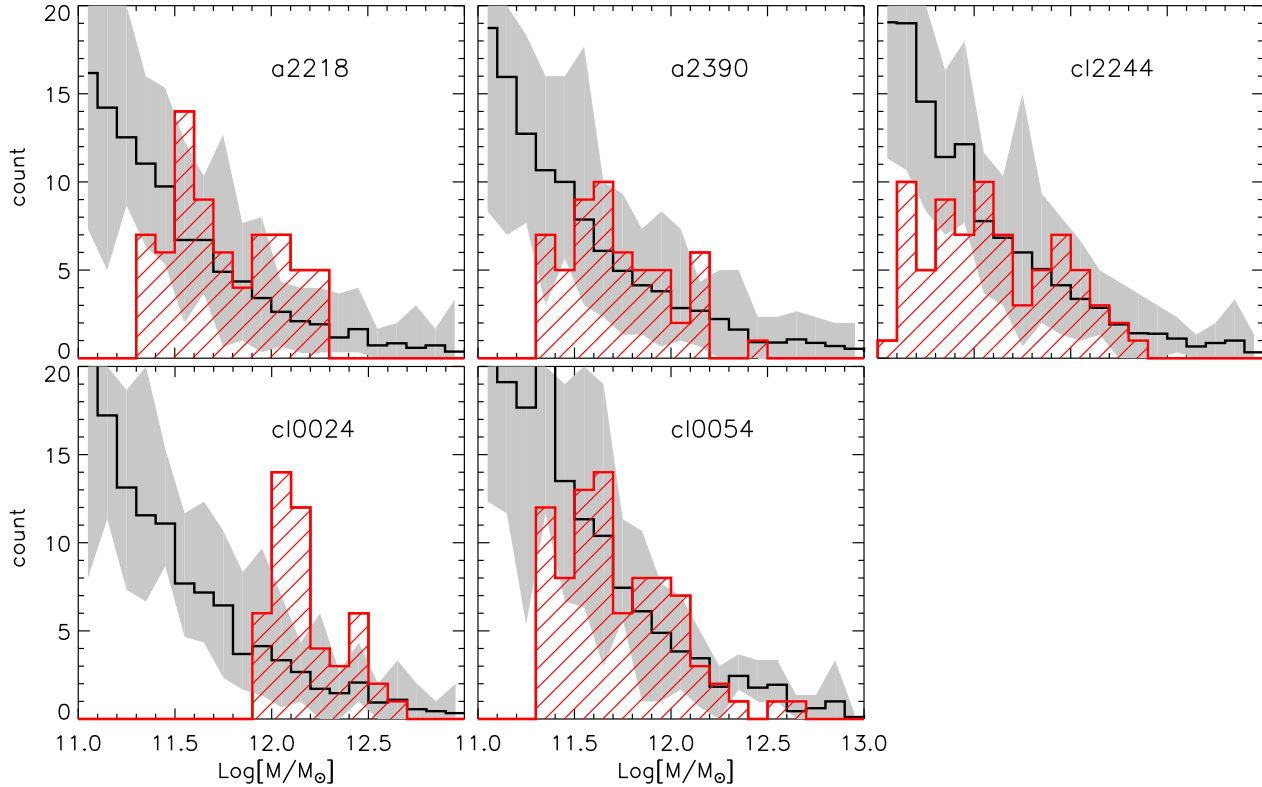


Figure 2. Comparison between substructure mass function retrieved from the galaxy-galaxy lensing analysis (red shaded histograms) and results from haloes selected from the Millennium Simulation. The black solid line in each panel represents the average subhalo mass function of haloes selected at the redshift of the observed lensing cluster (see text for details). The grey shaded region represents, for each value of the subhalo mass, the min-max number of substructures found in the simulated haloes.

rected for within the errors. It is interesting to note here that the only obvious outlier is Cl0024+16. This is the only system that clearly has a bimodal structure with two almost equal mass clumps separated by a small redshift offset. Its bimodal structure has been interpreted as a sign of a recent merger (Czoske et al. 2002). Clearly, if this is indeed the case, the comparison with relaxed massive haloes from the Millennium Simulation is not appropriate. We plan to investigate this question in more detail in future work by comparing the properties of the substructures in Cl0024+16 with clusters selected from the Millennium Simulation that are recent mergers of equivalent mass.

4.2 The distribution of velocity dispersions

In Fig. 3, we compare the distribution of velocity dispersions retrieved by the lensing analysis and the average distributions obtained for the simulated clusters selected from the Millennium Simulation. The velocity dispersions of substructures in simulated clusters are estimated using the velocity information for all the particles attached to the dark matter substructure and have been scaled by a factor of $\sqrt{2}$ (see previous section). Again we find generally a good agreement over the range sampled by the lensing analysis, except for Cl0024+16, which yet again appears to be an outlier (see discussion in previous section). Note here that the velocity dispersion retrieved from the lensing analysis

is one of the two parameters that characterises each subhalo. This velocity dispersion is the normalization of the Faber-Jackson relation, therefore, relates the mass (for the PIEMD model) to that of early-type galaxies. For the simulated haloes the measured velocity dispersion is that of the dark matter alone. We note that Springel et al. (2001) used a factor equal to 0.9 to convert the 1D dispersions of subhaloes into stellar velocity dispersions, which was adopted to match the zero-point of the Faber-Jackson relation. Due to the dissipation involved in star formation, it is plausible that the stellar velocity dispersion is *smaller* than that of the dark matter. On the other hand, we argued above that our mass estimates might be biased low. We explore spatial and velocity biases in more detail using the lensing results from A 2218 in a forthcoming paper.

4.3 The distribution function of tidal radii

We use the aperture radii derived from the lensing analysis as a proxy for the tidal radii for the subhaloes. These aperture radii are more compact than the tidally truncated extents of the subhaloes. This radius cannot be identified directly with the tidal radius defined in the usual sense, but is proportional to it. In Fig. 4, we finally show the comparison between the distribution of aperture radii (r_t) retrieved by the lensing analysis with the average distributions of the tidal radii of substructures in simulated clusters

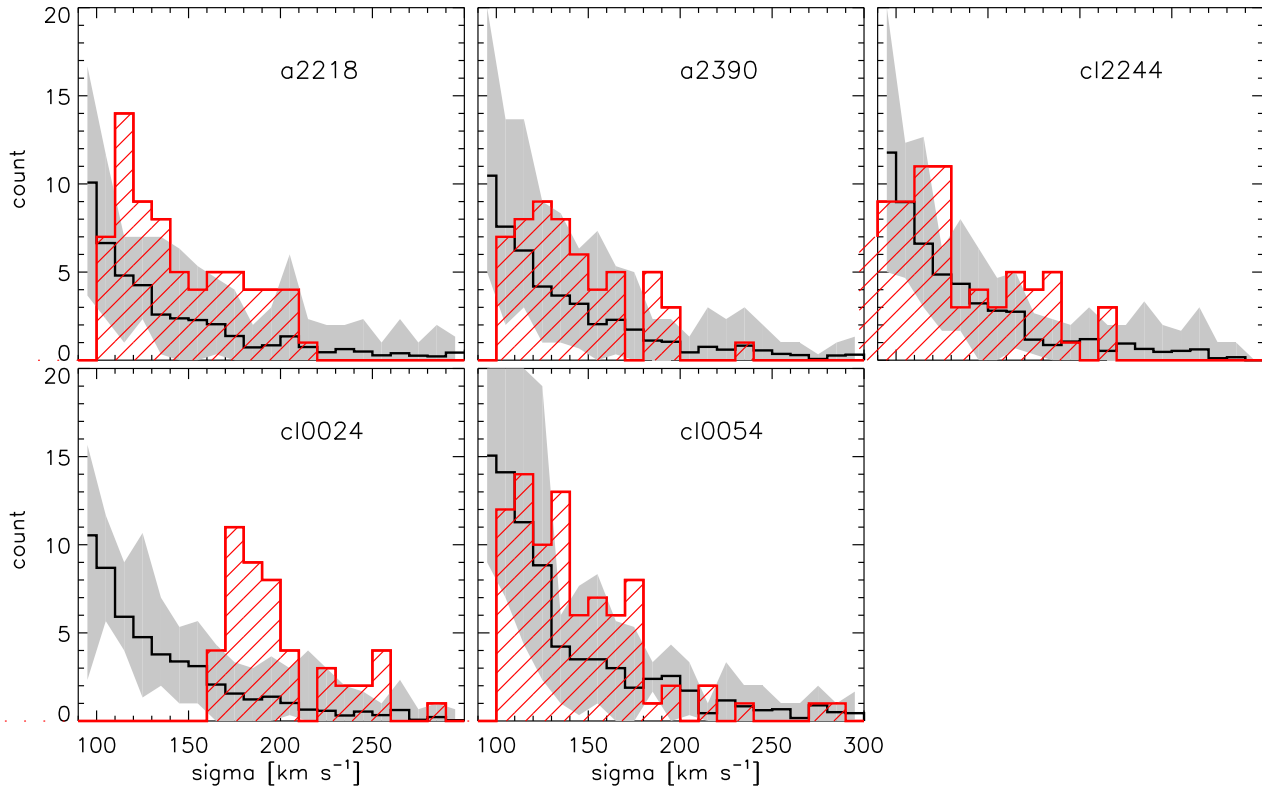


Figure 3. As in Fig. 2 but for the distribution of velocity dispersions.

selected from the Millennium Simulation. The solid black line in the figure and the grey filled region are obtained by measuring, for each substructure, the radius r_{half} that divides the halo mass in equal inner and outer parts. We note that, by using this measure of the radius, we find a very nice agreement with the distributions retrieved by the lensing analysis (with the usual exception of C10024+16) over the full range sampled by the observations. r_{half} , however, represents an underestimate of the ‘tidal radius’ of a dark matter substructure. The dashed black line in Fig. 4 gives the distribution obtained by using the radius corresponding to the maximum circular velocity (r_{max}), which is offset with respect to r_{half} by a factor that is slightly less than 2. We note that, as explained in the previous sections, the mass retrieved by the lensing analysis is essentially the mass within a fixed aperture, that is then identified as being proportional to the tidal radius of the associated dark matter substructure. Given the uncertainty in the measurement technique, the good agreement shown in Fig. 4 is therefore noteworthy. We recall that, in order to obtain a good agreement with the observed subhalo mass function, we have corrected their mass by a factor of 2. We are therefore in a situation where the substructures detected in the simulations are slightly bigger but less massive than those retrieved by our lensing technique. Such a situation would be expected if the density profiles assumed for the substructures are systematically denser in the inner parts than the simulated subhaloes. And, in fact, recent numerical studies suggest that dark matter subhaloes have softer profiles than NFW (Hayashi et al. 2004; Stoehr et al. 2003). Unfortunately our lensing tech-

nique is not sensitive to the choice of mass profile, rather it represents a tool to determine the total mass enclosed within an aperture. Higher resolution data will in the future allow the slopes of the mass profiles in substructure to be constrained.

5 CONCLUSIONS AND DISCUSSION

In this paper, we present (i) high resolution mass models for lensing clusters, (ii) the inferred mass function of subhaloes inside these clusters and (iii) a detailed comparison of the subhalo mass function, the velocity dispersion and aperture radii function with an ensemble of cluster-sized haloes selected from the Millennium Simulation. Detailed results of the application of our galaxy-galaxy lensing analysis techniques to five HST cluster lenses are used to construct high resolution mass models of the inner regions. In order to do so we have utilised both strong and weak lensing observations for these massive clusters. The goal has been to quantify substructure in the cluster assuming that the subhaloes follow the distribution of bright, early-type cluster galaxies. Similar attempts have been made in the lower density field environment yielding typical galaxy masses and central velocity dispersions. The mass distribution for a typical galaxy halo inferred from field studies are extended with no discernible cut-off. By contrast, in the cluster environments probed in this work we detect an edge to the mass distribution in cluster galaxies. We have performed various stringent checks to ascertain that this is not an artifact of the choice

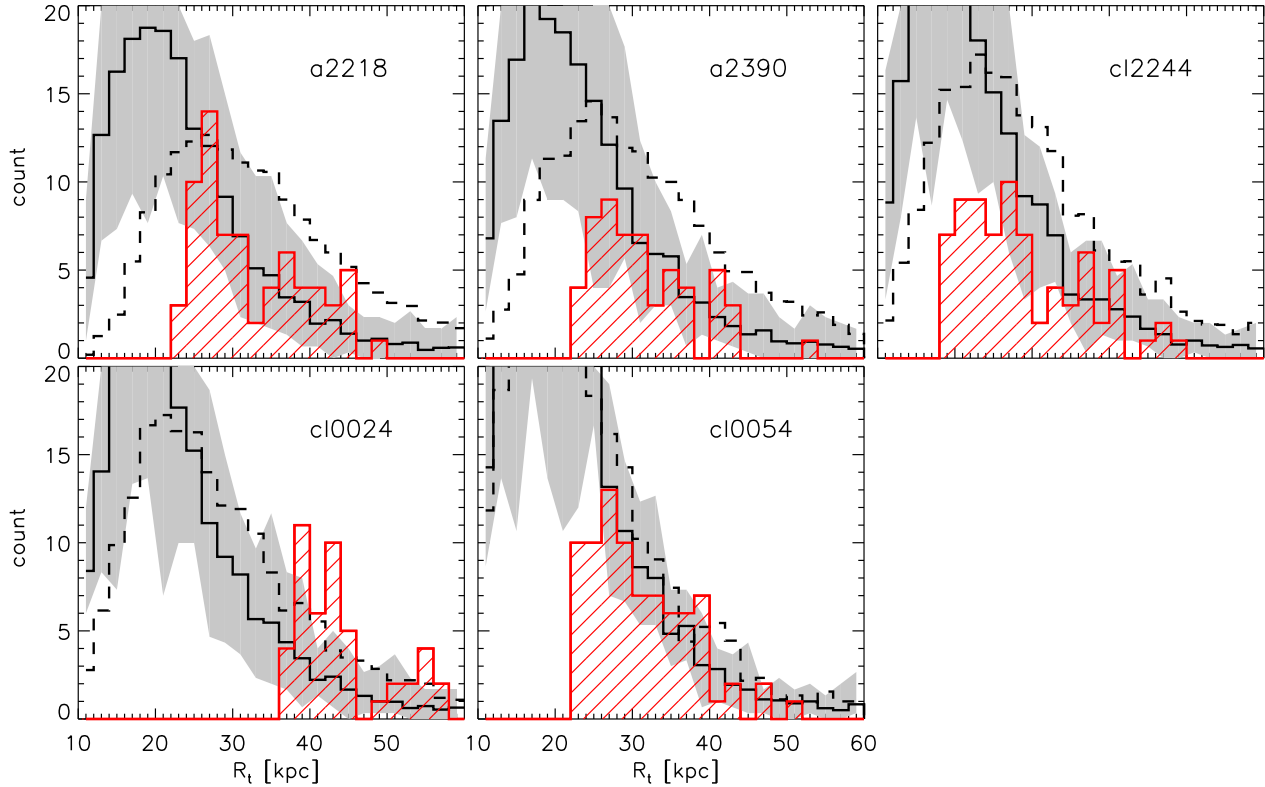


Figure 4. As in Fig. 2 but for the distribution of tidal radii. The solid black line with the grey regions are obtained by measuring for each substructure, the radius corresponding to its half mass. The dashed black line is obtained by taking the radius corresponding to the maximum circular velocity.

of mass model. Rather this result provides evidence for tidal stripping by the global cluster potential well.

Aside from the detailed lens models, we also present the mass spectrum (albeit within a limited mass range with subhalo masses ranging from $10^{11} - 10^{12.5} M_{\odot}$) of substructure in the inner regions of these clusters. The survival and evolution of substructure offers a stringent test of structure formation models within the CDM paradigm. Subhaloes of the size detected in all these clusters indicate a significant probability of galaxy–galaxy collisions over a Hubble time within a rich cluster. However, since the internal velocity dispersions of these clumps associated with early-type cluster galaxies ($\sim 150\text{--}250 \text{ km s}^{-1}$) are much smaller than their orbital velocities, these interactions are unlikely to lead to mergers, suggesting that the encounters of the kind simulated in the galaxy harassment picture by Moore et al. (1996) are the most frequent and likely. High resolution cosmological N-body simulations of cluster formation and evolution (De Lucia et al. 2004; Ghigna et al. 1998; Moore et al. 1996), find that the dominant interactions are between the global cluster tidal field and individual galaxies after $z = 2$. The cluster tidal field tidally strips galaxy haloes in the inner 0.5 Mpc efficiently and the radial extent of the surviving haloes is a strong function of their distance from the cluster centre. Much of this modification is found to occur between $z = 0$ and $z = 0.5$.

We have performed a detailed comparison of the subhalo mass function, velocity dispersion function and the dis-

tribution of aperture radii retrieved from lensing with an ensemble of massive clusters from the Millennium Simulation, which provides an ideal data-set for such an analysis. A series of systematic effects, due to the algorithm used to identify substructures in the simulation, needs to be taken into account when performing such a comparison. In addition, it should be kept in mind that the level of uncertainty of the observational results is still relatively high (for instance the mass derived from lensing is only accurate to within a factor of two and the technique is not sensitive to the choice of the substructure mass profile). Overall, we find consistency between the distribution of substructure properties retrieved using the lensing analysis and those obtained from simulations, although our detailed comparison seems to suggest that simulated substructures are slightly bigger but less massive than sub-clumps detected by means of lensing techniques. This might be due to systematic differences between the density profiles of simulated substructures and those assumed in the lensing model. Unfortunately, the technique is not sensitive to this choice but higher resolution data will allow in the future the slopes of the mass profiles in substructures to be constrained.

Despite the uncertainties mentioned above, the general agreement between simulations and results determined *independently* from lensing is remarkable. Our work represents a powerful test of the Λ CDM model, which at present appears to be consistent with the amount of observed substructure in massive, lensing clusters, up to redshifts of ~ 0.6 , given

the uncertainties. It will be very interesting to tighten the constraints with future lensing data.

ACKNOWLEDGEMENTS

The authors acknowledge Simon White for support and encouragement throughout this project. PN is grateful to the Virgo Consortium for access to the Millennium Simulation data. She acknowledges support from NASA via HST grant HST-GO-09722.06-A. She also thanks her collaborators Jean-Paul Kneib, Ian Smail and Richard Ellis for help with the observational data and useful input on the work. GDL thanks the Alexander von Humboldt Foundation, the Federal Ministry of Education and Research, and the Programme for Investment in the Future (ZIP) of the German Government for financial support.

REFERENCES

Aldering, G., et al., 2003, SPIE 4835, 40 (astro-ph/0209550)
 Allen, S., Ettori, S., & Fabian, A. C., 2001, MNRAS, 324, 877
 Benson, A. J., Frenk, C. S., Lacey, C. G., Baugh, C. M., & Cole, S. 2002, MNRAS, 333, 177
 Bertin, E., Arnouts, S., 1996, A&A, 117, 393
 Brainerd, T., Blandford, R., & Smail, I., 1996, ApJ, 466, 623
 Bruzual, G., & Charlot, S., 2003, MNRAS, 344, 1000
 Bullock, J. S., Kravtsov, A. V., & Weinberg, D. H. 2000, ApJ, 539, 517
 Couch, W.J., Barger, A.J., Smail, I., Ellis, R.S., Sharples, R.M., 1998, ApJ, 497, 188
 Clowe, D., & Scheider, P., 2002, A&A, 395, 385
 Couch, W.J., Shanks, T., & Pence, W.D., 1985, MNRAS, 213, 215
 Czoske, O., Moore, B., Kneib, J., & Soucail, G., 2002, A&A, 386, 31
 De Lucia, G., et al., 2004, MNRAS, 348, 333
 Diemand, J., et al., 2004, MNRAS, 352, 535
 Ebbels, T. M. D. et al., 2000, private communication.
 Farouki, R., & SHAPIRO, S. L., 1981, ApJ, 243, 32
 Fritz, A., et al., 2003, Ap&SS, 285, 61
 Frye, B., & Broadhurst, T., 1998, ApJ, 499, L115
 Gao, L., De Lucia, G., White, S. D. M., & Jenkins, A., 2004, MNRAS, 352, L1
 Ghigna, S., Moore, B., Governato, F., Lake, G., Quinn, T., & Stadel, J., 1998, MNRAS, 300, 146
 Gottlöber S., Klypin A. A., Kravtsov A. V., 1998, in Evolution of large-scale structure: From recombination to Garching, preprint, astro-ph/9810191
 Guzik, J., & Seljak, U., 2002, MNRAS, 335, 311
 Hayashi, E., Navarro, J. F., Power, C., Jenkins, A. R., Frenk, C. S., White, S. D. M., Springel, V., Stadel, J., & Quinn, T. R. 2004, MNRAS, 355, 794
 Hoekstra, H., Yee, H. K., & Gladders, M., 2004, ApJ, 606, 67
 Hudson, M. J., Gwyn, S. D. J., Dahle, H., & Kaiser, N., 1998, ApJ, 503, 531
 Holtzman, J., et al., 1995, PASP, 107, 156
 Kassiola, A., & Kovner, I. 1993, ApJ, 417, 474
 Kleinheinrich, M., et al., 2005, A&A, 439, 513
 Klypin, A., Kravtsov, A. V., Valenzuela, O., & Prada, F. 1999, ApJ, 522, 82
 Kneib, J-P., Ellis, R. S., Couch, W., Smail, I. R., & Sharples, R. 1996, 471, 643
 Kneib, J-P., et al., 2003, ApJ, 598, 804
 Kravtsov, A. V., Gnedin, O. Y., & Klypin, A. A. 2004, Apj, 609, 482

Le Borgne, J-F., Pello, R., & Sanahuja, B. 1992, A&AS, 95, 87
 Le Fevre, O., et al., 2004, A&A, 417, L839
 Limousin, M., Kneib, J-P., & Natarajan, P., 2005, MNRAS, 356, 309
 Limousin, M., et al., 2006, MNRAS, submitted
 Lynds, R., & Petrosian, V., 1998, ApJ, 336, L1
 Maller, A., & Bullock, J., 2004, MNRAS, 355, 694
 Merritt, D., 1983, ApJ, 264, 24
 McKay, T. et al. 2002, ApJ, 571, L85
 Miralda-Escude, J. 2002, ApJ, 564, 1019
 Moore, B., Katz, N., Lake, G., Dressler, A., & Oemler, A. 1996, Nature, 379, 613
 Moore, B., Ghigna, S., Governato, F., Lake, G., Quinn, T., Stadel, J., & Tozzi, P. 1999, ApJ, 524, L19
 Natarajan, P., & Kneib, J-P. 1997, MNRAS, 287, 833
 Natarajan, P., Kneib, J-P., Smail, I., & Ellis, R. S. 1998, ApJ, 499, 600
 Natarajan, P., Kneib, J-P., & Smail, I., 2002a, ApJ, 580, L11
 Natarajan, P., Loeb, A., Kneib, J-P., & Smail, I., 2002b, ApJ, 580, L17
 Natarajan, P., & Springel, V., 2004, ApJ, 617, L13
 Natarajan et al., 2006, in preparation
 Natarajan et al., 2006, submitted
 Okamoto, T., Habe, A., 1999, ApJ, 516, 591
 Ota, N., & Mitsuda, K., 2004, A&A, 428, 757
 Ota, N., Mitsuda, K., Fukazawa, Y., 1998, ApJ, 495, 170
 Pelló, R., et al., 1999, A&A, 343, L65
 Richstone, D., 1976, ApJ, 204, 642
 Schneider, P., & Rix, H-W., 1997, ApJ, 474, 25
 Sheldon, E., et al., 2004, A&A, 427, 2544
 Smail, I., et al., 1995, ApJ, 449, L105
 Smail, I., Dressler, A., Couch, W.J., Ellis, R.S., Oemler, A., Butcher, H., Sharples, R.M., 1997a, ApJS, 110, 213
 Smail, I., et al., 1997b, ApJ, 479, 70
 Smail, I., et al. 2001, MNRAS, 323, 839
 Smith, G. P., et al., 2005, 359, 417
 Spergel, D., & Steinhardt, P. J. 2000, Phys. Rev. Lett., 84, 17, 3760
 Springel, V., et al, 2001, MNRAS, 328, 726
 Stoeck, F., et al. 2003, MNRAS, 335, L84
 Tyson, J. A., Kochanski, G., & De'll Antonio, I. P., 1998, ApJ, 498, L107
 Weller, J., Ostriker, J., Bode, P & Shaw, L., 2005, MNRAS, 364, 283
 Wolf, C., et al., 2004, A&A, 421, 913
 Wilson, G., Kaiser, N., Luppino, G. A., & Cowie, L. L. 2001, ApJ, 555, 572
 Ziegler, B., et al., 2001, MNRAS, 325, 157

APPENDIX: LENSING ANALYSIS OF THE CLUSTERS

We briefly discuss the properties of the five lensing clusters that are studied here. The clusters in order of increasing redshift are: A 2218, $z = 0.18$; A 2390, $z = 0.23$; Cl 2244–02, $z = 0.33$; Cl 0024+16, $z = 0.39$; Cl 0054–27, $z = 0.57$. All clusters have multiple imaged background sources (some with several sets of multiple-imaged sources) with measured spectroscopic redshifts that are used to calibrate the overall mass model. In addition to these five clusters we will also include the results from our previous analysis of the rich cluster AC 114 at $z = 0.31$ described in Natarajan et al. (1998). The *HST* WFPC2 imaging of this cluster was analyzed and modeled in an identical manner to that used

here and hence allowing those results to be included in our discussion.

The X-ray and lensing properties of three of the clusters analyzed here (A 2218, Cl0024+16 and Cl0054–27) were discussed by Smail et al. (1997b) based on the data available at that time. We summarize the information from more recent observations of these clusters, as well as the two remaining systems (A 2390 and Cl 2244–02) below. The clusters range over an order of magnitude in terms of their X-ray luminosity ($L_X \sim 10^{43-44} h^{-2} \text{ erg s}^{-1}$) and roughly an order of magnitude in terms of their V-band luminosities ($L_V \sim 0.25-1 \times 10^{12} h^{-2} L_\odot$).

While these *HST* cluster-lenses span a large range in mass, richness, and X-ray luminosity, fortunately, they form a subset of clusters with morphologically well-studied galaxy populations (Couch et al. 1998; Smail et al. 1997a). For four of the clusters studied the morphological classification for the cluster members and cluster membership was obtained from the following sources: for AC 114 from Couch et al. (1998), for Cl 0024+16 and Cl 0054–27 from Smail et al. (1997a). We used only colour-selection to determine cluster membership and classification for A 2390 and Cl 2244–02.

The *HST* cluster lens sample

A 2218

A 2218 is one of the best-studied cluster lenses, with over 7 multiple-imaged background sources identified by *HST* observations (Kneib et al. 1996, 2004a, 2004b, Ellis et al 2001). The core of the cluster is dominated by a luminous cD galaxy and the galaxy population within the central $1 h^{-1} \text{ Mpc}$ is made up predominantly of morphologically classified early-type galaxies (Couch et al. 1998; Zeigler et al. 2001). *Chandra* observations of A 2218 yield a mean cluster temperature of $kT = 6.9 \pm 0.5 \text{ keV}$ and a rest-frame luminosity in the 2–10 keV energy band of $6.2 \times 10^{44} \text{ ergs s}^{-1}$ (Mahacek et al. 2002). The high-resolution *Chandra* data of the inner $2'$ of the cluster show that the X-ray brightness centroid is apparently displaced in projection from the cD galaxy. Asymmetric temperature variations are also detected along the direction of the cluster mass elongation. Although the X-ray and weak lensing mass estimates are in good agreement for the outer parts ($r > 200 h^{-1} \text{ kpc}$) of the cluster, in the inner region the observed X-ray temperature distribution is inconsistent with the assumption of the intra-cluster gas being in thermal hydrostatic equilibrium, pointing to recent merger activity.

A 2390

A 2390, at $z = 0.23$, is extremely luminous and hot in the X-rays. Recent *Chandra* measurements by Allen, Ettori & Fabian (2001) find an isothermal temperature distribution between $200 h^{-1} \text{ kpc}$ and $1 h^{-1} \text{ Mpc}$ with $kT = 11.5 \text{ keV}$, with a decline in the temperature within $200 h^{-1} \text{ kpc}$. This rich cluster has a significant early-type galaxy population that is concentrated in the inner regions (Fritz et al. 2003). The X-ray surface brightness profile is smooth and the optical data also suggest that the cluster is in dynamical equilibrium. The projected mass profile obtained from lensing, optical measurements of the galaxy velocity dispersions and

the X-ray data from *Chandra* are in good agreement (Allen, Ettori & Fabian 2001).

Cl 2244–02

Cl 2244–02 is a very compact cluster at $z = 0.33$ which produces a near complete Einstein ring image of a background galaxy at $z = 2.237$ (Lynds & Petrosian 1989), as well as a near-infrared selected giant arc (Smail et al. 1995). This remarkable lensing configuration confirms the massive mass concentration in the central regions of this cluster. The *HST* WFPC2 image reveals a very concentrated distribution of early-type galaxies in the inner 30 arcseconds, surrounded by the Einstein ring. However, there are relatively few obvious cluster galaxies outside this region. Moreover, the *ASCA* X-ray observations of the cluster by Ota et al. (1998) give $kT = 6.5 \pm 1.3 \text{ keV}$ and a rest-frame luminosity of just $1.3 \times 10^{44} \text{ erg s}^{-1}$ in the 2–10 keV band. The relatively low X-ray luminosity suggests that the cluster has a low mass, although the X-ray temperature indicates a more massive system. This is supported by the lensing model we have constructed for Cl 2244–02.

Cl 0024+16

The rich cluster Cl 0024+16 at $z = 0.39$ has a measured X-ray temperature of just $kT \sim 4.5 \text{ keV}$ (Ota et al. 2004). Ota et al. (2004) find that the surface brightness profile is represented by the sum of extended emission centred at the central bright elliptical galaxy with a small core of $\sim 50 \text{ kpc}$ and more extended emission with a core radius of $\sim 210 \text{ kpc}$. However, this is one of the cases where the mass determinations from three independent techniques, namely lensing, virial estimators, and X-ray data under the assumption of hydro-static equilibrium for the gas, were highly discrepant. Using spectroscopic information for about 300 galaxies within a projected radius of $3 h^{-1} \text{ Mpc}$ Czoske et al. (2002) examined the three-dimensional structure of this cluster and found that there are two dynamically distinct components separated by $\sim 3000 \text{ km s}^{-1}$ in velocity space. They argue that this is suggestive of a high-speed collision between these two sub-clusters. Such an interpretation would explain the origin of the disagreement between the various mass estimates. Recently published work by Kneib et al. (2003) using a panoramic sparsely sampled image from WFPC2 and STIS on *HST* derive a best-fit mass model from the lensing data out to $5 h^{-1} \text{ Mpc}$ in which they identified a secondary mass clump with about 30% of the overall cluster mass. Note that in this paper we construct a high-resolution mass model only for the inner region.

Cl 0054–27

The most distant cluster in our sample is Cl 0054–27 at $z = 0.57$. This is an optically-selected cluster with a dominant central galaxy (Couch et al. 1985). A multiple-imaged arc is visible in the *HST* images of this cluster with a measured a redshift of 3.2 for this feature (Leborgne, private communication). The X-ray luminosity of this cluster measured to be $2.5 h^2 10^{43} \text{ erg s}^{-1}$ in the 0.3 – 3.5 keV band,

Cluster	σ^* (km s ⁻¹)	r_t^* (kpc)	M_{ap}/L_v (M _⊙ /L _⊙)	M^* (10 ¹¹ M _⊙)	σ_{clus} (km s ⁻¹)	$\rho_{\text{clus}}(r = 0)$ (10 ⁶ M _⊙ kpc ⁻³)	
A 2218	0.17	180 ± 10	40 ± 12	5.8 ± 1.5	~ 14	1070 ± 70	3.95
A 2390	0.23	200 ± 15	18 ± 5	A 4.2 ± 1.3	~ 6.4	1100 ± 80	16.95
AC 114	0.31	192 ± 35	17 ± 5	6.2 ± 1.4	~ 4.9	950 ± 50	9.12
Cl 2244-02	0.33	110 ± 7	55 ± 12	3.2 ± 1.2	~ 6.8	600 ± 80	3.52
Cl 0024+16	0.39	125 ± 7	45 ± 5	2.5 ± 1.2	~ 6.3	1000 ± 70	3.63
Cl 0054-27	0.57	230 ± 18	20 ± 7	5.2 ± 1.4	~ 9.4	1100 ± 100	15.84

Table 1. Parameters that define the mass models of the subhaloes for the lensing clusters.

is lower than would be expected from the L_X to the measured shear strength correlation for massive lensing clusters (see Fig. 2 of Smail et al. 1997b for the correlation between L_X and $\langle g \rangle$ for a sample of HST cluster-lenses). Smail et al. (1997a) argue that this cluster is an example of a system that is elongated along the line-of-sight, leading to the low L_X for the measured surface mass density. Obviously, in cases like this the mass estimate obtained from X-ray data which assumes spherical symmetry is unlikely to provide accurate results.

Lensing Constraints

There are two aspects to constructing a successful lens model for the clusters analyzed here. Firstly, we must identify multiple-imaged background sources with reliable redshift measurements whose properties can be used to constrain the total projected mass within the lens models. Secondly, we have to extend these models to larger radii using the coherent distortion signal induced in the shapes of faint, background galaxies by the foreground cluster potential well.

Both of these steps use the deep, high-resolution imaging provided for the cluster cores by *HST*. All five clusters analyzed here were observed with WFPC2 on-board *HST* for Guest Observer programs GO 5352 (A 2390 and Cl 2244-02), 5378 (Cl 0054-27) 5453 (Cl 0024+16) and 5701 (A 2218). The filters used for the observations were F555W (V_{555}) and F814W (I_{814}) or F702W (R_{702}). Observations of A 2218 were taken in the R_{702} filter and all the other clusters studied here were observed in the I_{814} filter. We have used the colour information, when available, to test the identification of multiple-imaged sources in these fields. However, in the following analysis we use the reddest band available for a particular cluster to catalog objects and measure their shapes. The total exposure times are then 10.5 ks on both A 2390 and Cl 2244-02, 16.8 ks on Cl 0054-27 and 13.2 ks on Cl 0024+16, all in I_{814} , and 6.3 ks in R_{702} on A 2218. The individual exposures were generally grouped in sets of four single-orbit exposures each offset by 2.0 arcsec to allow for hot pixel rejection. After standard pipeline reduction, the images were aligned using integer pixel shifts and combined into final frames using the IRAF/STSDAS task CRREJ. We retain the WFPC2 colour system and hence use the zero points from Holtzman et al. (1995). The final images cover the central 0.8-1.6 Mpc of the clusters to a 5- σ point-source limiting magnitude of $I_{814} \sim 26.0$ or $R_{702} \sim 26.5-27.0$ (Smail et al. 1997a).

Multiple-imaged background galaxies have been identi-

fied using *HST* imaging and spectroscopically confirmed in A 2218 by Kneib et al. (1996, 2004b), in A 2390 by Pello et al. (1999) and Frye & Broadhurst (1998), Cl 2244-02 (Smail et al. 1995; Mellier et al. 1991), Cl 0024+16 by Broadhurst et al. (2000) and Cl 0054-27 by LeBorgne (priv. communication). These provide very strong constraints and drive the fit in the likelihood plane as we discuss below.

The second step in our analysis requires a statistical measure of the shear induced in the background field population. To achieve this we catalog faint objects in these frames and measure their shapes using the SEXTRACTOR image analysis package (Bertin & Arnouts 1995). Following Smail et al. (1997a, 1997b) we adopt a detection isophote equivalent to $\sim 1.3\sigma$ above the sky, where σ is the standard deviation of the sky noise, e.g. $\mu_{814} = 25.0$ mag arcsec⁻² or $\mu_{702} = 25.0$ mag arcsec⁻² for A 2218, and a minimum area after convolution with a 0.3 arcsec diameter top-hat filter of 0.12 arcsec². Analysis of our exposures provides catalogs of ~ 800 objects for each cluster across the 3 WFC chips. We discard the smaller, lower sensitivity, PC fields as well as a narrow border around each WFC frame in the following analysis. The imaging data (and catalogs) used here are identical to those previously analysed by Kneib et al. (1996) for A 2218, and Smail et al. (1997a, 1997b) for A 2218, Cl 0024+16 and Cl 0054-27. In order to account for the error in shapes produced due to PSF, we adopt a method similar to that of Smith et al. (2005).

To constrain the weak lensing aspect of the models of the various clusters we must construct well-defined samples of background galaxies for which image parameters can be measured with adequate signal-to-noise. For simplicity in modeling we have adopted uniform magnitude limits across the sample. The faint magnitude limit is determined by the depth at which reliable image shapes can be measured in our shortest exposures. This is $R_{702} = 26.0$, as set by the A 2218 exposure. The bright limit is set by our desire to reduce cluster galaxy contamination in the field samples for the most distant clusters and corresponds to a bright limit of $I_{814} = 22.5$. When converting between the R_{702} and I_{814} limited samples, we have assumed a typical colour for the faint field population at these depths of $(R_{702} - I_{814}) \sim 0.5$ (Smail et al. 1995b). Hence our background galaxy cut is defined simply as $R_{702} = 23-26$ or $I_{814} = 22.5-25.5$. Cluster galaxies are chosen with an additional luminosity cut-off.

Applying these limits yields a typical surface density of ~ 95 field galaxies per arcmin², in good agreement with that measured in genuine ‘blank’ fields ($\sim 95 \pm 10$ arcmin⁻²) after correcting for differences in the photometric systems

(Smail et al. 1995b). We thus estimate that any residual contamination in our catalogs from faint cluster members must be less than $\sim 5\text{--}10\%$. The final sample size in a typical cluster, after applying both the magnitude and the area cuts, is $\sim 350 - 400$ galaxies.

To determine the contribution to the observed shear from systematic effects in the *HST* optics, detectors, or the reduction method, we have also modeled the PSF anisotropy using the methods adopted by Smith et al. (2005) and corrected the background image shapes accordingly.

